

The investigation of the topographical effect on multi-scale Eastward-Moving Southwest Vortex from the perspective of PV theory

Chao Li¹, Yan Li², Shenming Fu³, Xingwen Jiang⁴, Xiaofang Wang⁵, Shanshan Li⁶, Chunguang Cui⁵, Yang Hu⁷, and Wenjun Cui⁸

¹Institute of Heavy Rain, CMA

²Lanzhou University

³Institute of atmospheric physics, Chinese Academy of Sciences

⁴Institution of plateau meteorology, China Meteorological Administration

⁵Institute of Heavy Rain, China Meteorological Administration

⁶Institute of Heavy Rain, CMA

⁷Institute of Heavy Rainfall, CMA, Wuhan, China

⁸University of Arizona

November 22, 2022

Abstract

Multi-scale Eastward-Moving Southwest Vortex (EMSV) inducing severe rainstorms frequently occurs in the middle and lower reaches of Yangtze River Basin (YRB). The Second-Step Terrain Region (SSTR) located in the middle reaches of YRB have significant role in strengthening this synoptic system. This paper systematically studies the topographical effect of SSTR based on the WRF synthetic simulation of three multi-scale EMSV cases that occurred in 2015 and 2016. Results show that the compound circulation simulated by WRF can be decomposed into the meso-scale balanced circulation and the local-scale perturbed circulation with the application of the Piecewise Potential Vortex Inversion (PPVI) technique. The cyclonic perturbed circulation has a closer relationship with the occurrence of local heavy precipitation compared to the balanced circulation. Moreover, the good agreement between the positive Potential Vortex (PV) anomalies and the cyclonic perturbed circulation suggests that the persistence of the cyclonic perturbed circulation highly depends on the positive PV anomalies. Besides, the qualitative sensitivity experiments reveal that the topographical effect stimulates the genesis of the positive PV anomalies mainly by strengthening the latent heat release associated with the updraft, and the latent heat release associated with the cyclonic eddy. The quantitative diagnosis of the source of the PV anomalies shows that the former one contributes more to the genesis of the positive PV anomalies than the latter one. Further quantitative diagnosis of the updraft reveals that the topographical lifting effect is identified as the main mechanism in strengthening the updraft within the topography region

1 **The investigation of the topographical effect on multi-scale**
2 **Eastward-Moving Southwest Vortex from the perspective of**
3 **PV theory**

4 Chao Li^{1,2}, Yan Li¹, Shenming Fu³, Xingwen Jiang⁴, Xiaofang Wang², Shanshan Li²,
5 Chunguang Cui², Yang Hu², Wenjun Cui⁵

- 6 1. College of Atmospheric Sciences, Lanzhou University, Lanzhou, China
7 2. Hubei Key Laboratory for Heavy Rain Monitoring and Warning Research, Institute of Heavy
8 Rain, China Meteorological Administration, Wuhan, China
9 3. Institute of Atmospheric Physics, Chinese Academy of Sciences, Beijing, China
10 4. Institute of Plateau Meteorology, China Meteorological Administration, Chengdu, China
11 5. Cooperative Institute for Mesoscale Meteorological Studies, Oklahoma University, Norman,
12 United States

13 **Abstract:** Multi-scale Eastward-Moving Southwest Vortex (EMSV) inducing severe rainstorms
14 frequently occurs in the middle and lower reaches of Yangtze River Basin (YRB). The
15 Second-Step Terrain Region (SSTR) located in the middle reaches of YRB have significant role in
16 strengthening this synoptic system. This paper systematically studies the topographical effect of
17 SSTR based on the WRF synthetic simulation of three multi-scale EMSV cases that occurred in
18 2015 and 2016. Results show that the compound circulation simulated by WRF can be
19 decomposed into the meso-scale balanced circulation and the local-scale perturbed circulation
20 with the application of the Piecewise Potential Vortex Inversion (PPVI) technique. The cyclonic
21 perturbed circulation has a closer relationship with the occurrence of local heavy precipitation
22 compared to the balanced circulation. Moreover, the good agreement between the positive
23 Potential Vortex (PV) anomalies and the cyclonic perturbed circulation suggests that the
24 persistence of the cyclonic perturbed circulation highly depends on the positive PV anomalies.
25 Besides, the qualitative sensitivity experiments reveal that the topographical effect stimulates the
26 genesis of the positive PV anomalies mainly by strengthening the latent heat release associated
27 with the updraft, and the latent heat release associated with the cyclonic eddy. The quantitative
28 diagnosis of the source of the PV anomalies shows that the former one contributes more to the
29 genesis of the positive PV anomalies than the latter one. Further quantitative diagnosis of the
30 updraft reveals that the topographical lifting effect is identified as the main mechanism in
31 strengthening the updraft within the topography region.

32 **1. Introduction**

33 The mesoscale convective activities are highly active within the latitudinal zone

34 of 30° N, where most of Yangtze River Basin (YRB) is located (Zheng, et al., 2008;
35 Yang, et al., 2015; Cui et al., 2020). Different terrains distributed within YRB have
36 important effects on the generation and reinforcement of mesoscale convective
37 activities. The Eastward-Moving Southwest Vortex (EMSV) as typical Mesoscale
38 Convective Vortex (MCV) originates from the southeastern slope of Tibetan Plateau,
39 and have close relationship with the evolution of Mesoscale Convective Systems
40 (MCSs). These two different scales of weather systems are frequently coupled (i.e.
41 multi-scale EMSV system) and evolved into multi-scale EMSV system during the
42 eastward-moving of Southwest Vortex. The Second-Step Terrain Region (SSTR)
43 (marked with red dashed rectangle in Fig.1), a typical type of topography located in
44 the middle reaches of YRB, plays critical roles in generating and strengthening the
45 EMSV and the associated MCSs. Subsequently the reinforced EMSV and MCSs take
46 dominant responsibilities for the frequent occurrence of severe rainstorms in the
47 middle and lower reaches of YRB (Zhang et al., 2019). Therefore, further
48 investigation of the topographical effect exerted by the SSTR is demanded for full
49 understanding of the reinforcement mechanism of the multi-scale EMSV system, as
50 well as the triggering mechanism of the local heavy precipitation.

51 It is frequently observed that the MCSs and the MCVs are mutually coupled in
52 many local heavy precipitation events (Davis, et al., 2009). Previous study have
53 confirmed that the genesis of MCV can be induced by the adiabatic cooling released
54 by an MCS in the middle level of troposphere, whereas the advantageous ambient
55 conditions provided by MCV is contrarily favorable for the prolongation of the

56 lifespan of MCSs (Houze, 2004). The MCV (Southwest Vortex is a typical type of
57 MCV) and MCSs incorporated in the multi-scale EMSV system respectively regulate
58 different scales of ambient circulation fields, and they have different responses to the
59 topographical force of SSTR when the multi-scale EMSV system passed over SSTR,
60 which subsequently brings more complexity to the interaction mechanism between
61 MCVs and MCSs. Therefore, it is essential to investigate how the topographical effect
62 affects the evolution of the Southwest Vortex and MCSs respectively based on the
63 effective decomposition of the compound circulation incorporated into the multi-scale
64 EMSV system into different scales of circulation that represent Southwest Vortex and
65 MCSs, so that more accurate understanding of the topographical effect on the local
66 heavy precipitation can be achieved.

67 Potential Vortex (PV) is a compound physical variable that can be applied to
68 describe both dynamic and thermal properties of the atmospheric motion, which was
69 first proposed by Rossby (1940). The PV theory is widely adopted in the analysis and
70 diagnosis of the synoptic system due to its conservative property and inversion
71 property. However, PV anomalies will be generated with non-adiabatic and frictional
72 condition, then focus on revealing how the PV anomalies are generated can help
73 advance the understanding of the evolution mechanism of some particular types of
74 synoptic systems. Previous study reveals that the non-adiabatic heating and the
75 frictional effect of the underlying surface are the direct causes for the genesis of the
76 PV anomalies (Haynes, et al., 1987; Raymond, et al., 1992). And the non-adiabatic
77 heating causes PV anomalies mainly by the following physical processes, including

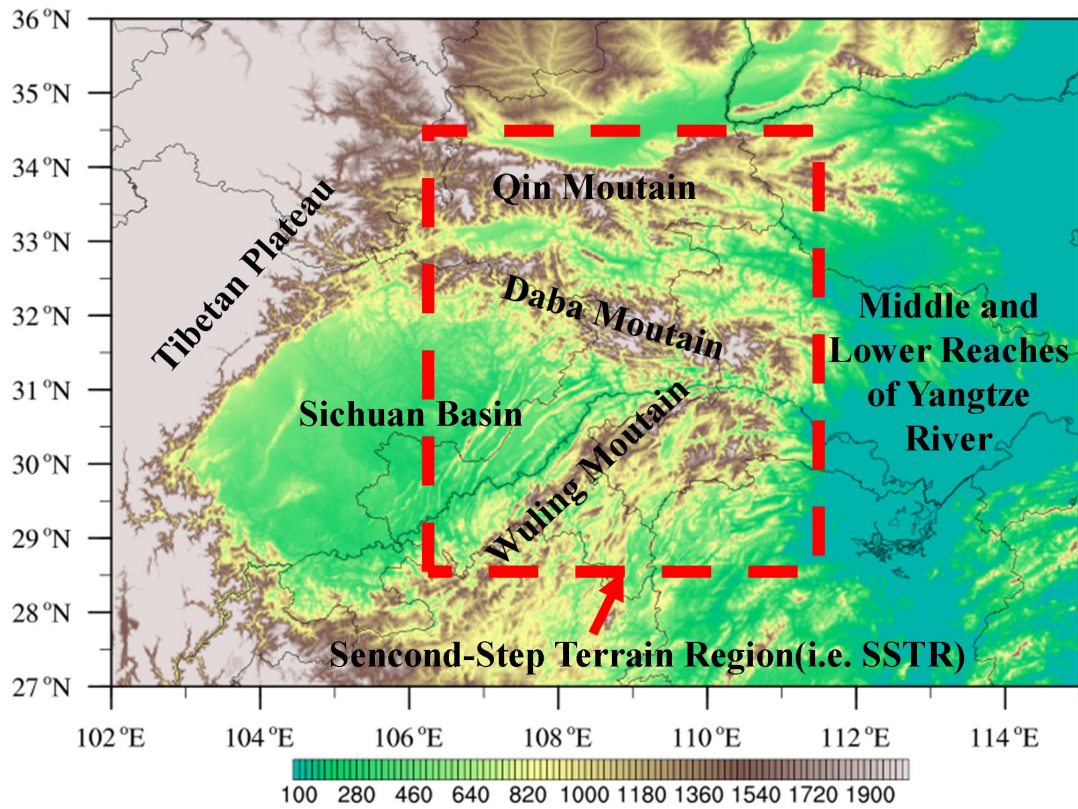
78 the latent heat release associated with the convection, the evaporation on the ground
79 surface and the moisture condensation within the cloud. With exception of the above
80 factors, the topographical effect is another key factor for the genesis of the PV
81 anomalies. The PV anomalies can be generated by the breaking of the wave train in
82 the leeward of mountain, or by the split of the incident flow over the terrain,
83 subsequently the Von Karman vortex streets appear under the co-effect between the
84 PV anomalies in the air and the potential temperature anomalies on the ground surface,
85 and the persistence of the vortex streets provides favorable condition for the
86 occurrence of the subsequent severe convective weather (Schar,et al.,1997). Further
87 research discovered that the dynamical structure of PV anomalies band is closely
88 related with the topographical feature and the dynamic processes dominated by the
89 topographical effect (Schar,et al.,2003), which reconfirms the importance of the
90 topography in affecting the generation and the structure of PV anomalies. Therefore,
91 analyzing the topographical effect from the perspective of PV theory is a
92 recommendable approach to gain more in-depth understanding of the topographical
93 effect on multi-scale EMSV system.

94 The technique of Piecewise Potential Vortex Inversion (PPVI) is established
95 based on the inversion property of PV, which provides an effective approach to
96 decompose the compound circulation into different types of circulation. The PPVI
97 technique was first proposed by Eliassen and Klenschmidt(1957), and this innovative
98 discovery demonstrated excellent prospect in the diagnosis and the prediction of the
99 synoptic scale and the mesoscale of atmospheric motion at that time. Hoskins (1985)

100 presented detailed elaboration of the physical meaning of PPVI targeting for the
101 practical application, building a solid foundation for the widespread application of
102 PPVI. Different scales of circulation incorporated in some particular multi-scale
103 synoptic systems, such as typhoon systems, Meiyu front systems, mesoscale vortex
104 systems, are feasible to be abstracted from the compound circulation with PPVI. The
105 further analysis of the decomposed circulations can help advance the understanding of
106 the evolution mechanism of these high impact weather systems(Wang, et al., 2005;
107 Zhang, et al., 2006; Zhao, et al., 2006; Ge, et al., 2011). Besides, to quantitatively
108 diagnose the contribution of different types of circulation to the evolution of the
109 coupling synoptic system based on the PPVI technique is another significant
110 application of PPVI (Chen, et al., 2003; Fu, et al., 2019).

111 The complexity of the interaction mechanism between multi-scale EMSV
112 systems and the topographical effect of SSTR results in the uncertainty of the
113 topographical effect on the evolution of multi-scale EMSV systems. Therefore,
114 advancing the understanding of the topographical effect of SSTR on the
115 reinforcement of multi-scale EMSV system is in great demand as the enhanced
116 multi-scale EMSV system often leads to catastrophic heavy rainfall events. To address
117 this scientific issue, the following three steps are conducted in this paper: Step 1 is to
118 select several representative multi-scale EMSV cases with similar origin locations,
119 cyclonic circulation scale, and moving direction, and then conduct synthetic
120 simulation based on the synthesis of these selected cases; Step 2 is to decompose the
121 compound circulation of the multi-scale EMSV system simulated by the WRF model

122 into different scales of circulation, and investigate the evolution characteristics of
123 these different scales of circulation under the topographical effect of SSTR; Step 3 is
124 to investigate the linkage between these different scales of circulation and the
125 distribution of PV anomalies induced by the topographical effect of SSTR; In Step 4,
126 through qualitative sensitivity experiments and quantitative diagnosis, we will reveal
127 the mechanism of how the PV anomalies are generated under the topographical effect
128 of SSTR.



129 Fig. 1 The topographical map of the middle reaches of Yangtze River (The red dashed rectangle denotes the range of the Second-Step
130 Terrain Region, shaded color denotes the altitude, unit: m)

131 2. Dataset and methodology

132 The primary data applied in this paper includes the Final Operational Global
133 Analysis (FNL) data from National Centers For Environmental Prediction (NCEP)

134 with 6 h temporal and $1^{\circ} \times 1^{\circ}$ spatial resolution, and the hourly fusion precipitation
135 data merged from the rain gauge data and the CMORPH satellite data from the
136 National Meteorological Information Center of China Meteorological Administration
137 (NMIC/CMA). Since the accuracy of the gauge-based analysis relies on both density
138 and configuration of the gauge network and the interpolation method. Thus
139 satellite-based precipitation products generated by combining passive microwave
140 (PMW) and infrared (IR) sensors are particularly useful over poorly gauged regions as
141 they are capable in detecting spatial patterns and temporal variations of precipitation
142 at a finer resolution. The improved datasets with hourly temporal resolution can better
143 capture the variations of heavy weather events (Shen, et al. 2014).

144 Since the analysis of the topographical effect is based on the synthesis of the
145 selected cases, the synthesis criterion needs to be first ascertained. Here, the synthesis
146 approach mainly refers to taking the average of the selected cases at corresponding
147 time respectively. As the start time, the end time and the lifespan for the selected cases
148 are completely different from each other, the identification of the reference time (RT)
149 for the synthesis of different cases becomes crucial. The RT in this paper is defined as
150 the moment when the geopotential height center of EMSV on 700 hPa isobaric
151 surface first enters the specified range (marked with blue rectangle in Fig.2). Then the
152 synthesis results can be achieved by taking the average of the selected cases according
153 to the RT and every 6 hours interval after RT. Furthermore, the initial field and the
154 lateral boundary field to drive the WRF simulation of the synthesized multi-scale
155 EMSV system can be provided by the above synthesis results. The detailed settings of

156 the physical parameters in the WRF model are shown in Table 1 (Mlawer, et al., 1997;
157 Dudhia, 1989; Hong, et al., 2006; Jimenez, et al., 2012; Milbrandt, 2005).

158 The PPVI theory shows superiority in the diagnosis of the thermal and dynamical
159 processes of the mesoscale vortex circulation due to its conservation and inversion
160 properties (Eliassen, et al., 1957). The key process to study the topographical effect of
161 SSTR in this paper highly depends on the decomposition of the compound circulation
162 incorporated in the multi-scale EMSV system, and the decomposition of the
163 compound circulation incorporated in the multi-scale EMSV system into different
164 scales of circulation is fundamentally based on the PPVI technique, so it is essential to
165 present detailed elaboration of the principle of the PPVI theory in this paper.

166 Ertel's PV is a conservative variable on the premise of the
167 frictionless and adiabatic heating condition (Rossby, 1940; Ertel, 1942), which is:

$$168 \quad q = \frac{1}{\rho} \zeta_a \cdot \nabla \theta \quad (1.1)$$

169 where q is Ertel's PV, ρ is the air density, ζ_a is the absolute vorticity, ∇ is the
170 three-dimensional gradient operator, and θ is the potential temperature.

171 The quasi-geostrophic balance equation was first established by Charney (1955)
172 to describe the quasi-geostrophic motion for free atmosphere, which is:

$$173 \quad \nabla^2 \phi = \nabla \cdot f \nabla \psi + 2 \left[\frac{\partial^2 \psi}{\partial x^2} \frac{\partial^2 \psi}{\partial y^2} - \left(\frac{\partial^2 \psi}{\partial x \partial y} \right)^2 \right] \quad (1.2)$$

174 where ϕ is the potential function, ψ is the stream function, and f is geostrophic

175 parameter.

176 If the horizontal wind defined in the Ertel's PV is replaced by the non-divergent
177 wind and non-rotation wind, Eq 1.1 can be substituted with stream function ψ and
178 potential function ϕ , which is:

$$179 \quad q = \left[(f + \nabla^2 \psi) \frac{\partial^2 \phi}{\partial z^2} - \frac{\partial^2 \psi}{\partial z \partial x} \frac{\partial^2 \phi}{\partial z \partial x} - \frac{\partial^2 \psi}{\partial z \partial y} \frac{\partial^2 \phi}{\partial z \partial y} \right] \quad (1.3)$$

180 where ψ , ϕ , and q are compound variables here, which can be regarded as the
181 constitution of the balanced component and the perturbed component, which are:

$$182 \quad \psi' = \psi - \bar{\psi}, \quad \phi' = \phi - \bar{\phi}, \quad q' = q - \bar{q} \quad (1.4)$$

183 where $\bar{\psi}$ and $\bar{\phi}$ denote the balanced component of the variables, which represent
184 the temporal average, while ψ' and ϕ' denote the perturbed component of the
185 variables, which represent the surplus between the compound component and the
186 balanced component.

187 For linearizing Eq. 1.2 and Eq. 1.3, these two equations are substituted with Eq.
188 1.4, and the final forms of Eq. 1.2 and Eq. 1.3 with simplified operations are
189 presented as following:

$$190 \quad \nabla_h^2 \phi' = f \nabla_h^2 \psi' + \beta \frac{\partial \psi'}{\partial y} + 2 \left(\frac{\partial^2 \bar{\psi}}{\partial x^2} \frac{\partial^2 \psi'}{\partial y^2} - 2 \frac{\partial^2 \bar{\psi}}{\partial x \partial y} \frac{\partial^2 \psi'}{\partial x \partial y} + \frac{\partial^2 \bar{\psi}}{\partial y^2} \frac{\partial^2 \psi'}{\partial x^2} \right) \\ + 2 \left(\frac{\partial^2 \psi'}{\partial x^2} \frac{\partial^2 \psi'}{\partial y^2} - \left(\frac{\partial^2 \psi'}{\partial x \partial y} \right) \right) \quad (1.5)$$

$$\begin{aligned}
q' = & \left(f + \nabla_h^2 \bar{\psi} \right) \frac{\partial^2 \phi'}{\partial z^2} + \nabla_h^2 \bar{\psi}' \cdot \frac{\partial^2 \bar{\phi}}{\partial z^2} - \frac{\partial^2 \bar{\psi}}{\partial x \partial z} \frac{\partial^2 \phi'}{\partial x \partial z} - \frac{\partial^2 \bar{\psi}}{\partial y \partial z} \frac{\partial^2 \phi'}{\partial y \partial z} - \frac{\partial^2 \bar{\psi}'}{\partial x \partial z} \frac{\partial^2 \bar{\phi}}{\partial x \partial z} - \frac{\partial^2 \bar{\psi}'}{\partial y \partial z} \frac{\partial^2 \bar{\phi}}{\partial y \partial z} \\
& + \nabla_h^2 \bar{\psi}' \cdot \frac{\partial^2 \phi'}{\partial z^2} - \frac{\partial^2 \bar{\psi}'}{\partial x \partial z} \frac{\partial^2 \phi'}{\partial x \partial z} - \frac{\partial^2 \bar{\psi}'}{\partial y \partial z} \frac{\partial^2 \phi'}{\partial y \partial z}
\end{aligned} \tag{1.6}$$

192 The variables of q' , f , $\bar{\psi}$, $\bar{\phi}$ in the above equations can be calculated out
 193 based on the WRF simulation results, while the variables of $\bar{\psi}'$ and $\bar{\phi}'$ in Eq. 1.5 and
 194 Eq. 1.6 are the only two remaining variables that are waiting for solution. Since Eq.
 195 1.5 and Eq. 1.6 jointly build up closed equations regarding $\bar{\psi}'$ and $\bar{\phi}'$, thus the
 196 variables of $\bar{\psi}'$ and $\bar{\phi}'$ can be surely solved. And the perturbed horizontal wind U' and
 197 V' can be solved by the combination of $\bar{\psi}'$ and $\bar{\phi}'$, while the balanced horizontal
 198 wind \bar{U} and \bar{V} can be solved by the combination of $\bar{\psi}$ and $\bar{\phi}$.

199 Table 1. The settings of the physical parameters in WRF simulation

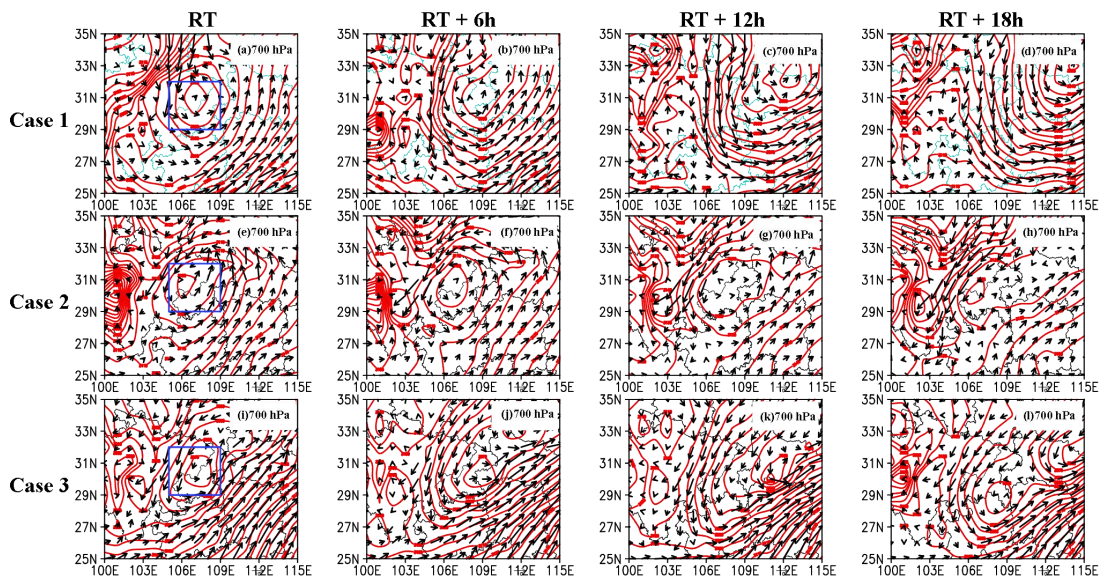
Horizontal		Microphysics	Longwave	Shortwave	Surface	Land	Boundary	Cumulus
Resolution	Grid Number	Scheme	Radiation	Radiation	Layer	Lurface	Layer	Convective
			Scheme	Scheme	Scheme	Scheme	Scheme	Scheme
		Milbrandt-						
		Yau	RRTM	Dudhia	Monin-Obu	Thermal	MYNN 2.5	Betts-Miller
9km	630×400	2-moment	scheme	Scheme	khov	diffusion	level TKE	-Janjic
		scheme			scheme	scheme	scheme	scheme

200 3. Case study background

201 3.1 The observed background circulation of each selected case

202 In order to reveal the topographical effect of SSTR on multi-scale EMSV systems,
 203 three representative cases with similar origin location, similar cyclonic circulation
 204 scale, and similar moving direction are selected from those high impact events
 205 occurred during 2015-2016. In details, the event for Case 1 approximately started at

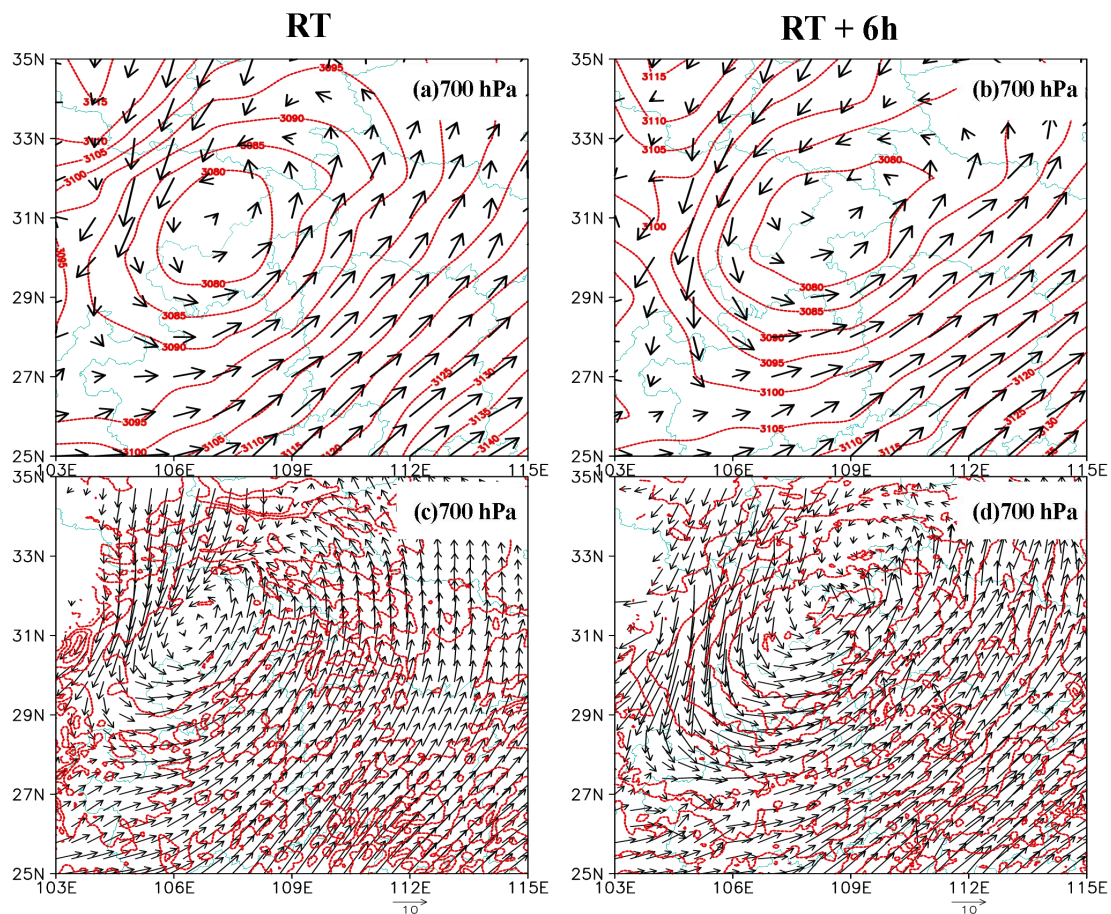
206 1800UTC on April 30th and ended at 0000UTC on May 2nd in 2015, the event for
 207 Case 2 approximately started at 0000UTC on August 18th and ended at 0600UTC on
 208 August 19th in 2015, and the event for Case 3 approximately started at 0000UTC on
 209 June 30th and ended at 0600UTC on July 1st in 2016. Fig. 2 shows the evolution
 210 characteristics of the background circulation of these selected cases. These selected
 211 cases can be synthesized into a whole one due to their common features, which is
 212 capable in reflecting the common evolution characteristics of this type of EMSV
 213 systems under the topographical effect of SSTR. As the reinforcement of multi-scale
 214 EMSV system and the increase in local precipitation intensity are mainly
 215 concentrated during the period from RT to RT+6h, this period is the main concerned
 216 stage in this paper naturally.



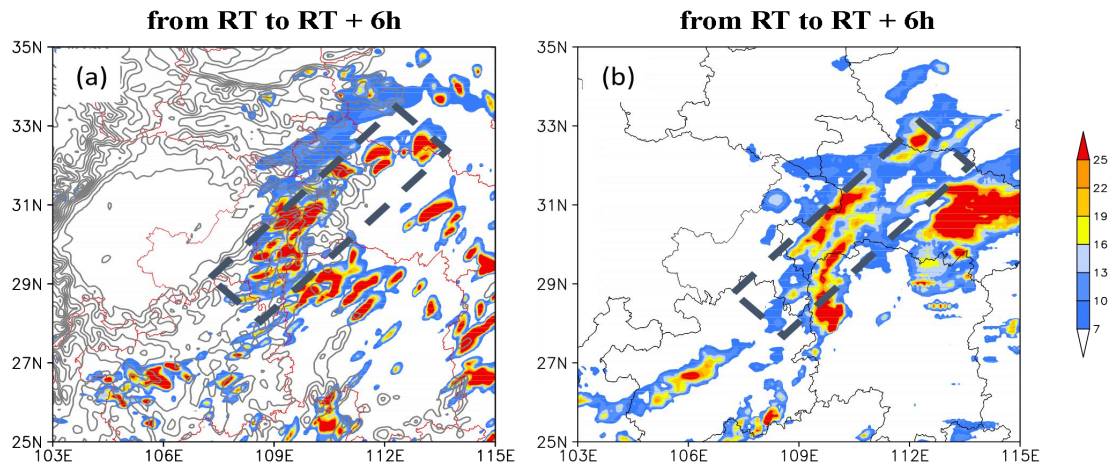
217 Fig. 2 The observation of wind (black vector, unit: m/s) and geopotential height (red contour, unit: gpm) derived from different cases of
 218 multi-scale EMSV systems on the isobaric surface at 700 hPa (a-d: Case 1; e-h: Case 2; i-l: Case 3)

219 **4. Assessment of the synthesized simulation capacity**

220 It is demonstrated in Fig.3 that the synthesized simulation is capable in
 221 reflecting the key features of the synthesized multi-scale EMSV system. To be
 222 specific, the location of the multi-scale EMSV systems and the evolution of the
 223 cyclonic circulation simulated by WRF agree well with the observation (Fig.3).
 224 Besides, despite the disparities of the distribution of the precipitation between the
 225 WRF simulation and the observation (located in the east and center of Hubei
 226 Province), the local heavy precipitation distributed along the Wuling Mountain
 227 (marked with gray rectangle in Fig.4) still demonstrates good agreement between the
 228 WRF simulation and the observation. On account of the realistic representation of the
 229 multi-scale EMSV systems and the local heavy precipitation, it is practicable to adopt
 230 the WRF simulation to further investigate the topographical effect of SSTR.



231 Fig. 3 The horizontal wind (black vector, unit: m/s) and the altitude (red contour, unit: m) of the observations (a, b) from the synthesis of
232 the whole selected cases and the WRF simulation (c, d) at the moment of RT (left column) and RT+6h (right column) on the isobaric
233 surface at 700 hPa



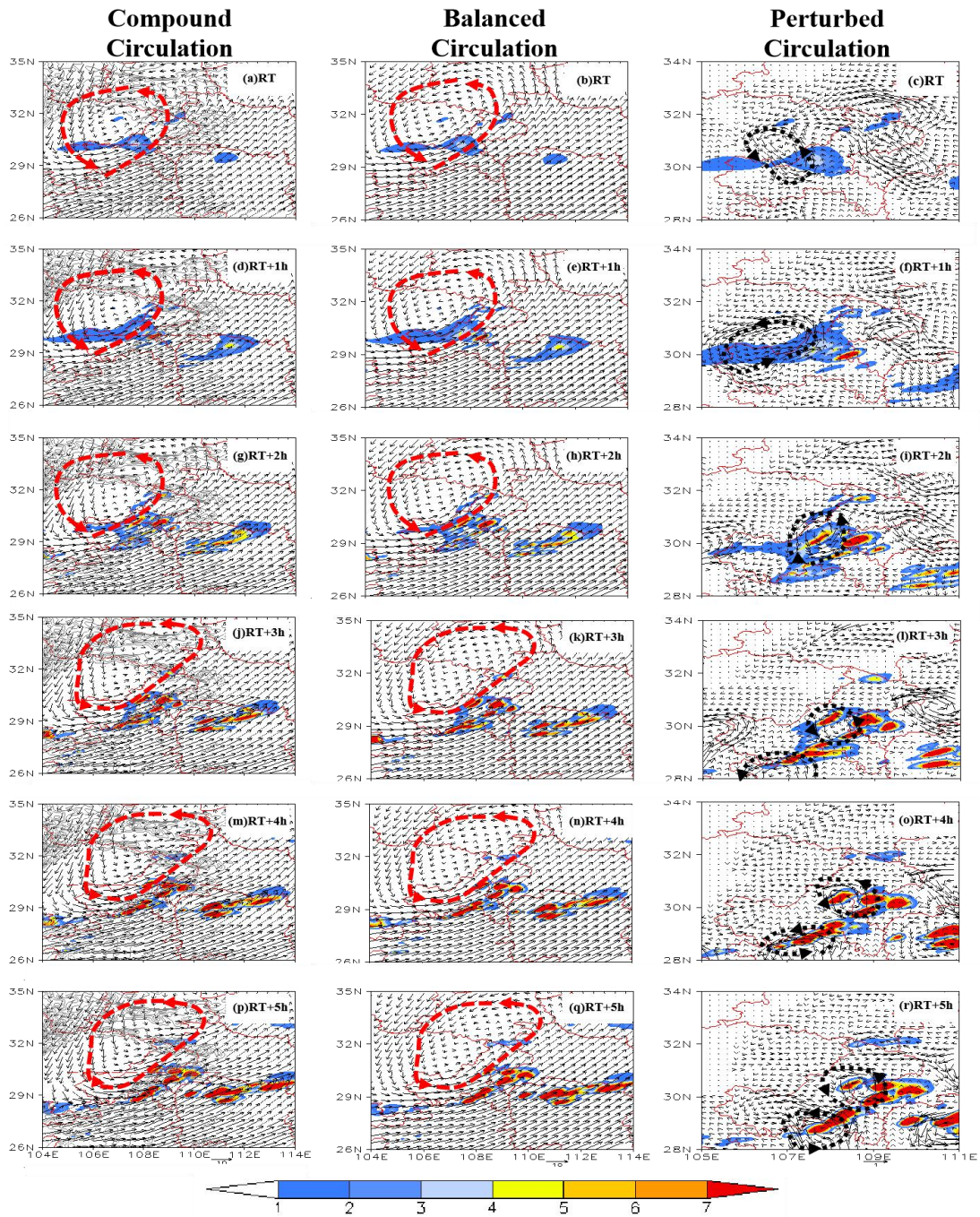
234 Fig.4 Comparison of the accumulated precipitation (colored, unit: mm) between the synthesized WRF simulation (a) and the
235 synthesized CMORPH observation (b) during the period from RT to RT+6h (the gray contour in panel a represents the topographic isoline
236 that exceeds over 800 m, the interval is 200 m)

237 5. Results

238 5.1 Decomposition of the compound circulation based on PPVI

239 From the perspective of PPVI theory, the compound circulation simulated by
240 WRF primarily includes two different scales of circulation: the balanced circulation
241 and the perturbed circulation. The balanced circulation is regulated by the balanced
242 component of the stream function and the potential function, whereas the perturbed
243 circulation highly depends on the perturbed component of the stream function and the
244 potential function (more details presented in Section 2). It is clearly demonstrated in
245 Fig. 5 that the balanced circulation can well capture the slow evolution of the meso- α
246 scale cyclonic circulation (marked with red dashed vectors in the second column) in
247 the multi-scale EMSV system, and the balanced circulation almost has no alteration
248 when the local precipitation is intensified. In comparison, the perturbed circulation

249 can well characterize the quick replacement of the local scale cyclonic circulation
250 (marked with black dashed vectors in the third column) in the multi-scale EMSV
251 system, which has good agreement with the reinforcement of the local precipitation
252 intensity. Moreover, under the co-effect of the southwesterly wind dominated by the
253 Southwest Vortex and the topographical effect of SSTR, most of the local heavy
254 precipitation areas are approximately located along the Wuling Mountain. The meso- α
255 scale balanced circulation guarantees the abundant water vapor transportation, which
256 provides the essential moisture condition for the occurrence and the persistence of the
257 local heavy precipitation. However, the local scale perturbed circulation around the
258 heavy precipitation area takes direct responsibility for the occurrence of the local
259 heavy precipitation and provides the fundamental dynamical condition for the
260 intensification of the local precipitation. Considering the close relationship between
261 the perturbed circulation and the local heavy precipitation, identifying the factors that
262 determine and regulate the replacement of the perturbed circulation is the key issue
263 that needs to be addressed subsequently.

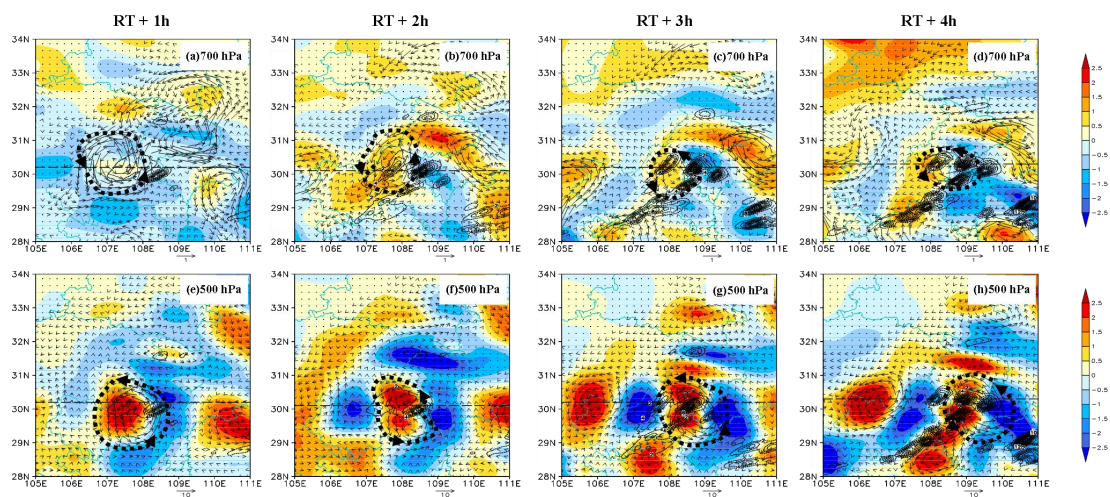


264 Fig. 5 Spatial distributions of hourly accumulated precipitation simulated by WRF (colored, unit: mm) and decomposition of the mixed
 265 circulation simulated by WRF (first column, vector, unit: m/s) into the balanced circulation (second column, vector arrow, unit: m/s) and
 266 the perturbed circulation (third column, vector arrow, unit: 10^{-1} m/s) during the period from RT to RT+5h on 700 hPa isobaric surface

267 **5.2 The good agreement between PV anomalies and perturbed circulation**

268 The illustration of PPVI theory in Section 2 indicates that the perturbed
 269 circulation can be solved by the combination of the perturbed stream function and the

270 perturbed potential function, and both are closely associated with the perturbed PV,
271 thus further investigation is needed to study the relationship between the perturbed
272 circulation and the perturbed PV (defined as the PV anomalies here). It is shown in
273 Fig. 6 that the PV anomalies and the perturbed circulation show good agreement with
274 each other, especially around the local heavy precipitation area. The cyclonic
275 perturbed circulation (marked with the black dashed vectors) happens to appear in the
276 positive PV anomalies zone, which is observed on both 700 hPa isobaric surfaces (Fig.
277 6a - 6d) and 500 hPa isobaric surfaces (Fig. 6e - 6h). The stronger positive PV
278 anomalies (denoted by colored) do cause stronger cyclonic perturbed circulation
279 (marked with black dashed vectors) by the contrast between 700 hPa isobaric surface
280 and 500 hPa isobaric surface. What should be paid more attention to is that the
281 windward slope region is the most noticeable location where the positive PV
282 anomalies are generated remarkably. Moreover, since the main concern and interest of
283 the study is to reveal the topographical effect, it is essential to identify whether the
284 topographical effect will lead to the formation of the positive PV anomalies. Further
285 investigation on the mechanism of how the positive PV anomalies are generated
286 within the topography region may help advance the understanding of topographical
287 effect of SSTR.

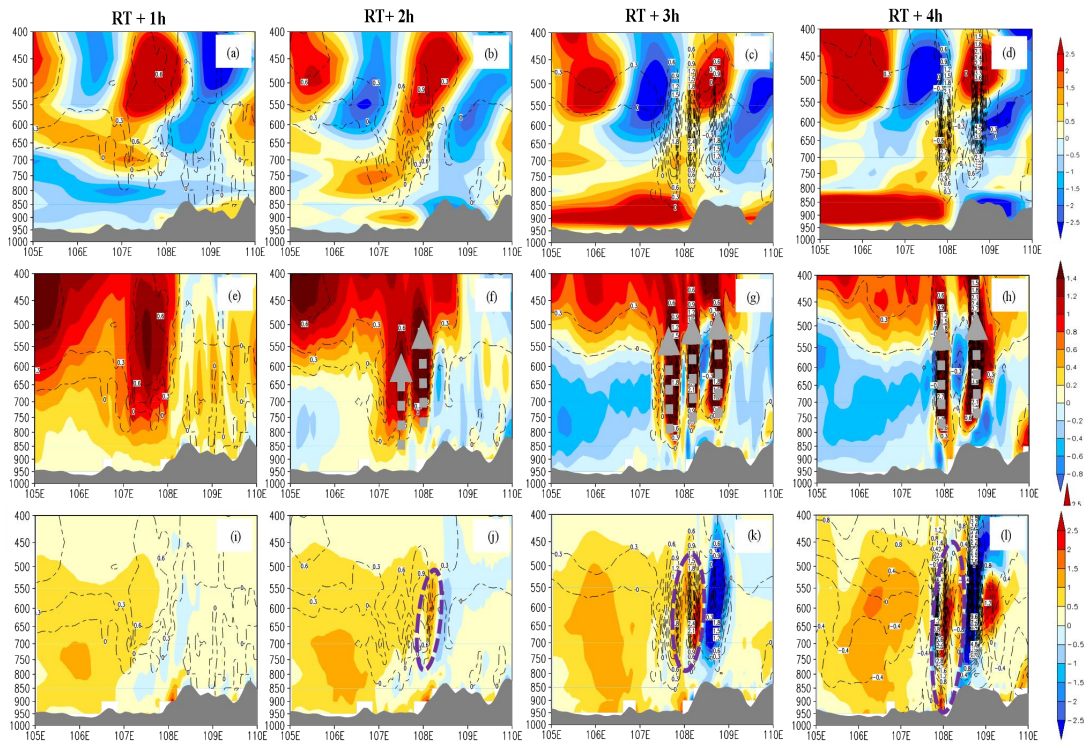


288 Fig. 6 Spatial distributions of the perturbed wind (black vectors, unit: m/s) and the PV anomalies (colored, unit: PVU, 1 PVU=
 289 $10^{-6} \cdot \text{K} \cdot \text{s}^{-1} \cdot \text{Kg}^{-1}$) on 700 hPa (a-d) and 500 hPa (e-h) isobaric surface (The black dashed line marks the location of the profile presented in
 290 the following section)

291 5.3 The vertical distribution of PV anomalies and its relevant variables

292 Previous study clearly pointed out that the PV anomalies are fundamentally
 293 determined by the variables including the potential temperature associated with the
 294 latent heat release, the cross-isentropic transport by the vertical wind and the absolute
 295 vorticity, which are incorporated in a diagnosed equation regarding the temporal
 296 variability of PV (Raymond, 1992). The vertical distributions of these variables
 297 demonstrate good agreement with each other in Fig. 7. From the figure, we can see
 298 that the increase of the latent heat release (contour in Fig.7a - 7d) is favorable for the
 299 genesis of positive PV anomalies (colored in Fig.7a - 7d), and the topographical effect
 300 of the windward slope does promote the increase of the latent heat release, which
 301 subsequently leads to stronger positive PV anomalies in the lower level of troposphere.
 302 In addition, it is confirmed that the vertical transportation of water vapor by the
 303 updraft (colored in Fig.7e - 7h) is directly responsible for the latent heat release

304 (contour in Fig.7e - 7h), and the topographical effect of the windward slope
 305 strengthens the updraft by the topographical lifting mechanism (denoted by gray
 306 dashed vectors in Fig. 7e - 7h), which accordingly results in the increase of the latent
 307 heat release. Moreover, positive feedback mechanism between the vertical wind
 308 (marked with contour line in Fig. 7i - 7l) and the relative vorticity (marked with
 309 shaded color in Fig. 7i - 7l) is observed as the changes in these two variables are well
 310 correlated with each other. The vertical stretch of the relative vorticity in the
 311 windward slope resulting from the blocking of the windward slope further promotes
 312 the strengthening of the updraft, causing more latent heat release and resulting in
 313 stronger positive PV anomalies indirectly.

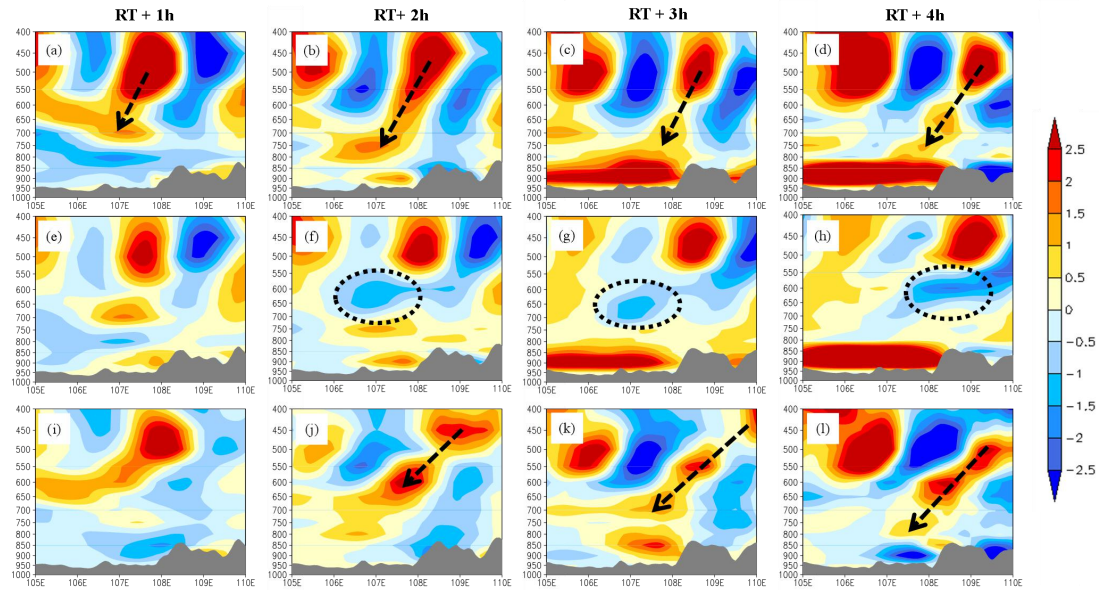


314 Fig. 7 Vertical profiles of the PV anomalies (colored in a - d, unit: PVU, 1 PVU=10⁻⁶ K·s⁻¹·Kg⁻¹), the latent heat release (black dashed
 315 contour in a - h, unit: kg/J), the vertical wind (colored in e - h, black dashed contour in i - l, unit: m/s), and the relative vorticity (colored
 316 in i - l, unit: 10⁴ s⁻¹)

317 **5.4 Sensitivity experiments on different factors associated with the PV anomalies**

318 **5.4.1 Sensitivity experiment on the role of the latent heat release**

319 A sensitivity experiment on the latent heat release (Fig. 8) is designed to further
320 verify the critical role of the latent heat release in the genesis of the positive PV
321 anomalies. The results show that the downward expansion of the positive PV
322 anomalies is broken down with no latent heat release in the windward slope region
323 (the black dashed oval in Fig. 8f - 8h). Moreover, the promotion of the positive PV
324 anomalies by the latent heat release is nearly limited in the middle and low levels of
325 troposphere (below 550 hPa isobaric surface). In other words, the positive PV
326 anomalies in the high level of troposphere (above the isobaric surface of 550 hPa)
327 seem to be less influenced by the removal of the latent heat release in the sensitivity
328 experiment, which means the latent heat release is not the dominant factor for the
329 generation of the positive PV anomalies in the high level of troposphere. In summary,
330 the increase of the latent heat release induced by the topographical effect can promote
331 the continuous genesis of the positive PV anomalies in the middle and low level of
332 troposphere and the downward expansion of positive PV anomalies, which
333 accordingly guarantees the persistence of the cyclonic perturbed circulation in these
334 levels of troposphere.

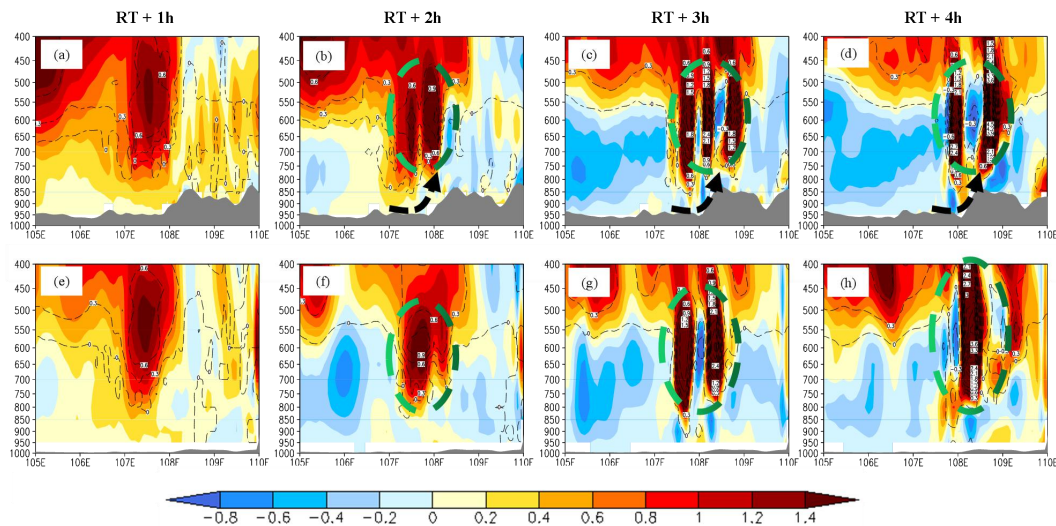


335 Fig. 8 Sensitivity experiment on the effect of the latent heat release on the genesis of PV anomalies in the vertical profile(a - d: control
 336 experiment; e - h: sensitivity experiment with no the latent heat release; i - l: the difference between the control experiment and the
 337 sensitivity experiment; colored: PV anomalies, unit: PVU, $1 \text{ PVU} = 10^{-6} \cdot \text{K} \cdot \text{s}^{-1} \cdot \text{Kg}^{-1}$)

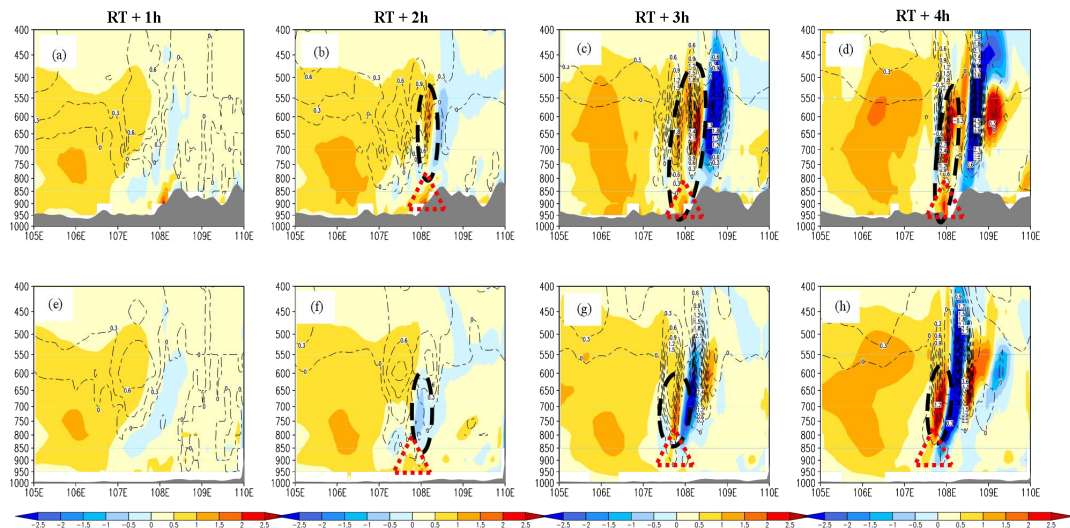
338 5.4.2 Sensitivity experiment on the topographical effect of the windward slope

339 As the significant topographical effect on the genesis of the positive PV
 340 anomalies is confirmed in previous section, the sensitivity experiment on the
 341 topographical elevation is designed to explore how the topographical effect associated
 342 with topographical elevation influences those key factors that are crucial for the
 343 genesis of the positive PV anomalies, including the velocity of the vertical wind, the
 344 latent heat release, and the relative vorticity. The difference between the control
 345 experiment and the sensitivity experiment indicates that the strength of the updraft
 346 (colored in the dashed oval in Fig. 9) in the windward slope region is remarkably
 347 weakened from the middle level to the low level of troposphere, and the latent heat
 348 release (black dashed line in the dashed oval in Fig. 9) is weakened accordingly with
 349 the removal of the topography in the sensitivity experiment. Besides, the blocking of

350 air mass in front of the windward slope region causes the reinforcement of the relative
 351 vorticity (colored in the dashed triangle in Fig. 10). Similarly, the relative vorticity is
 352 weakened likewise with the removal of the topography in the sensitivity experiment.
 353 Furthermore, the stretch of the relative vorticity resulting from the blocking of the
 354 windward slope does contribute to the strengthening of the updraft (black dashed line
 355 in the dashed oval in Fig. 10) from the middle level to the low level of troposphere in
 356 the control experiment, while the updraft is significantly weakened as the relative
 357 vorticity decreases in the sensitivity experiment.



358 Fig. 9 Sensitivity experiment of the terrain elevation on the velocity of vertical wind (colored, unit: m/s) and the latent heat release
 359 (black dashed line, unit: kg/J) in the vertical profile (a - d: control experiment; e - h: sensitivity experiment in which the terrain elevation
 360 is reduced by ten times)

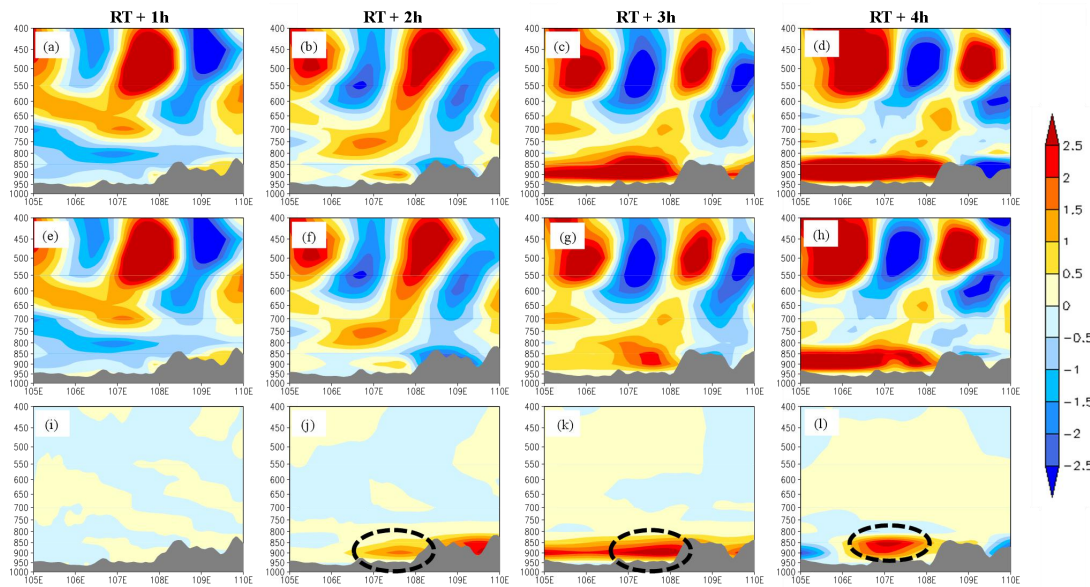


361 Fig. 10 Sensitivity experiment of the terrain elevation on the velocity of vertical wind (black dashed line, unit: m/s) and the relative
 362 vorticity (colored, unit: 10^4 s^{-1}) in the vertical profile (a - d: control experiment; e - h: sensitive experiment in which the terrain elevation
 363 is reduced by ten times)

364 5.4.3 Sensitivity experiment on the surface frictional dissipation

365 As the surface frictional dissipation is another significant factor for the generation
 366 of the PV anomalies, the sensitivity experiment on the surface friction is designed to
 367 verify the role of the surface friction in the genesis of the PV anomalies. It is
 368 demonstrated in Fig.11 that the genesis of the PV anomalies weakens with the friction
 369 velocity ust^* (ust^* is applied in the PBL scheme of WRF to describe the effect of
 370 surface friction on the atmosphere) increased by five times in the sensitivity
 371 experiment, which indicates that the effect of the surface frictional dissipation has
 372 negative feedback on the generation of PV anomalies. Moreover, we can see from the
 373 figure that the influence of the surface frictional dissipation is strictly limited below
 374 850 hPa (black dashed oval in Fig.11), meanwhile the effect of the surface frictional
 375 dissipation is not the primary inducement to the generation of the positive PV
 376 anomalies in the middle and high levels of troposphere. In conclusion, the above

377 sensitive experiment suggests that when we investigate which factor has the major
 378 impact on the genesis of the positive PV anomalies above 850 hPa isobaric surface,
 379 the surface frictional dissipation effect on the genesis of PV anomalies can be
 380 neglected as the positive PV anomalies are less influenced by the frictional effect
 381 therein.



382 Fig. 11 Sensitivity experiment of the surface frictional dissipation effect on the genesis of the PV anomalies in the vertical profile (a - d:
 383 control experiment; e - h: sensitivity experiment in which the friction velocity increased by five times; i - l: difference between the control
 384 experiment and the sensitivity experiment; colored: PV anomalies, unit: PVU, $1 \text{ PVU} = 10^{-6} \cdot \text{K} \cdot \text{s}^{-1} \cdot \text{Kg}^{-1}$)

385 5.5 Quantitative diagnosis of the source of the PV anomalies

386 A series of sensitivity experiments are designed to discuss the roles of these
 387 above factors in the generation of PV anomalies. However, the results of these
 388 sensitivity experiments are mainly qualitative, only affirming the indispensable roles
 389 of these factors in the genesis of PV anomalies. Hence, more detailed quantitative
 390 diagnosis of the topographical effect is required to identify which factor plays the

391 dominant role in the generation of PV anomalies. The factors including the adiabatic
 392 heating by the latent heat release, the vertical advection driven by the vertical wind,
 393 the horizontal advection driven by the eddy flow and the surface frictional dissipation
 394 effect (Raymond, et. al, 1990; Raymond, 1992; Peter et. al, 1999) are all taken into
 395 consideration to systematically establish a diagnosed equation (shown as Eq. 2.3)
 396 regarding the temporal variability of PV. Then the contributions of these factors to the
 397 temporal variability of PV are precisely assessed based on this quantitative diagnosed
 398 equation.

399 The diagnosed equation regarding the temporal variability of PV is presented as
 400 the following:

$$401 \quad \frac{dq}{dt} = \rho^{-1} \nabla \cdot (H \zeta_a + \nabla \theta \times F) \quad (2.1)$$

402 Where q is the potential vortex, F is the friction, ζ_a is the absolute vorticity, θ is the
 403 potential temperature. H in Eq. 2.1 represents the adiabatic heating rate, which can be
 404 furthered defined as:

$$405 \quad H = w \left(\frac{\partial \theta_p}{\partial z} \right) \quad (2.2)$$

406 where w represents the velocity of vertical wind, then Eq. 2.1 is substituted with Eq.
 407 2.2, and the final form with simplification is given below:

$$408 \quad \frac{dq}{dt} = \rho^{-1} \zeta_z \left(\frac{\partial w}{\partial z} \right) \frac{\partial \theta_p}{\partial z} + \rho^{-1} w \left(\frac{\partial \zeta_a}{\partial z} \right) \frac{\partial \theta_p}{\partial z} + \rho^{-1} \nabla \cdot (\nabla \theta \times F) \quad (2.3)$$

\downarrow
 ①

\downarrow
 ②

\downarrow
 ③

409

410 Where the three different terms ①, ②, ③ are corresponding to the absolute vorticity
411 term targeted for the characterization of the latent heat release driven by the horizontal
412 eddy flow, the vertical velocity term targeted for the characterization of the latent heat
413 release driven by the vertical wind, and the friction term targeted for the
414 characterization of the frictional dissipation effect respectively.

415 As previous sensitivity experiment has confirmed that the effect of the surface
416 frictional dissipation on the genesis of the PV anomalies can be neglected above 850
417 hPa isobaric surface, and the quantitative diagnosis is focused on revealing the
418 genesis mechanism of the PV anomalies above 850 hPa isobaric surface, thus the
419 quantitative diagnosis regarding the frictional dissipation term can be ignored here.
420 More details of the quantitative diagnosis of the absolute vorticity term and the
421 vertical velocity term are shown in Fig.12. In the early period (the period from RT+1h
422 to RT+2h), the contributions of the absolute vorticity term and the vertical velocity
423 term both keep in a low level. And in the later period (the period from RT+3h to
424 RT+4h), the level of the contribution of the two terms almost have no alteration in the
425 region that is distant from the topography region, while the level of the contribution of
426 the two terms have a remarkable growth within the topography region, moreover, the
427 contribution of the vertical velocity term is slightly higher than that of the absolute
428 vorticity term. On the whole, the positive value of the sum of these two terms within
429 the topography region guarantees the genesis of the positive PV anomalies within the
430 topography region, which is consistent with the findings revealed in the topography
431 sensitivity experiment. Further investigation reveals the linkage between the vertical

432 velocity term and the absolute vorticity term. To be specific, the blocking of the
433 windward slope leads to the accumulation of the air at the foot of the mountain, which
434 in turn forces the updraft associated with the vertical velocity term to intensify,
435 resulting in the reinforcement of the ambient wind convergence based on the
436 continuity of atmospheric motion, and the cyclonic eddy flow associated with the
437 absolute vorticity term gradually arises and strengthens accompanied by the
438 reinforcement of the ambient wind convergence accordingly.

439 Due to the critical role of the vertical wind in determining the temporal variability
440 of PV, further quantitative diagnosis is performed to reveal the mechanism of how the
441 topographical effect affect the variation of the vertical wind. It is reported in previous
442 study (Yue, et al., 2013) that the topographical effect has two fundamental
443 mechanisms to generate or reinforce the vertical wind, one is the topographical lifting
444 effect, and the other is the boundary layer convergence effect. These two effects are
445 both taken into account to establish a quantitatively diagnosed equation to investigate
446 the linkage between the topography and the vertical wind. The diagnosed equations
447 are presented below:

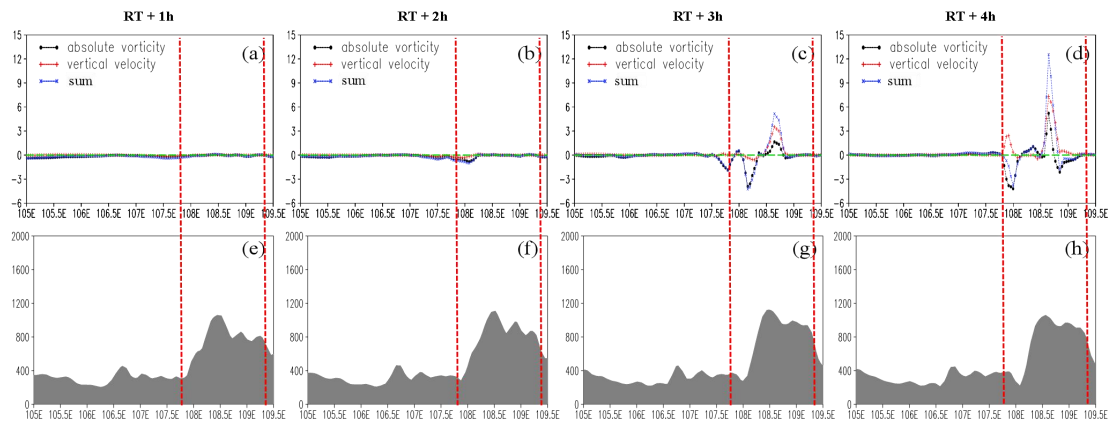
$$448 \quad W = W_L + W_F \quad (3.1)$$

449 where W_L is the vertical wind driven by the topographical lifting effect, W_F is the
450 vertical wind driven by the boundary layer convergence effect, and these two terms
451 can be further defined as:

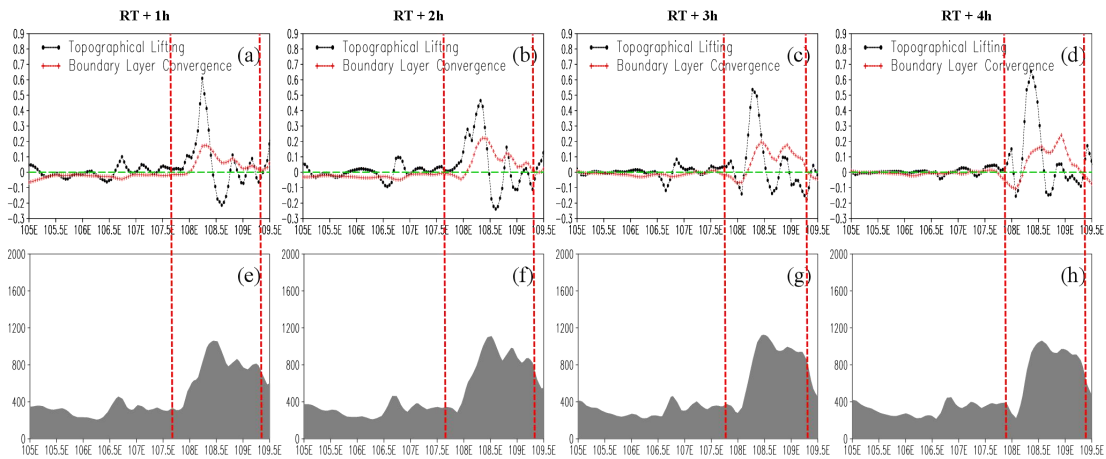
$$452 \quad W_L = u \frac{\partial h}{\partial x} + v \frac{\partial h}{\partial y} \quad (3.2)$$

$$W_F = \frac{1}{f} \left[\frac{\partial}{\partial x} (C_d v \sqrt{u^2 + v^2}) - \frac{\partial}{\partial y} (C_d u \sqrt{u^2 + v^2}) \right] \quad (3.3)$$

454 Where h in Eq. 3.2 is the topography elevation, f in Eq. 3.3 is the geostrophic
 455 parameter, which is constant for the mesoscale and microscale atmospheric motion
 456 over the mid-latitude zone, and C_d in Eq. 3.3 represents the drag coefficient, which is
 457 constant as well. Then the quantitative diagnosis of these two different effects is
 458 performed based on Eq. 3.2 and Eq. 3.3 respectively, and the results are shown in Fig.
 459 13. It is shown that the vertical wind driven by the topographical lifting effect and the
 460 boundary layer convergence effect both have remarkable growth within the
 461 topography region. However, the strengthening of the vertical wind driven by the
 462 topographical lifting effect is significantly higher than that driven by the boundary
 463 layer convergence effect. This suggests that the topographical lifting effect of the
 464 windward slope is the dominant mechanism to generate the positive PV anomalies
 465 that are responsible for the persistence of the cyclonic perturbed circulation, while the
 466 boundary layer convergence effect becomes the secondary one accordingly.



467 Fig. 12 Quantitative diagnosis of the absolute vorticity term (a-d, black line, unit: $10^{-5} \cdot K \cdot s^{-2} \cdot Kg^{-1}$), the vertical velocity term (a-d, red
 468 line, unit: $10^{-5} \cdot K \cdot s^{-2} \cdot Kg^{-1}$) and the sum of these two terms (a-d, blue line, unit: $10^{-5} \cdot K \cdot s^{-2} \cdot Kg^{-1}$) regulated by the topography (e - h, unit: m)
 469 to the genesis of the PV anomalies on 700 hPa isobaric surface (The red dashed line marks the range of topography region)



470 Fig. 13 Quantitative diagnosis of the vertical wind speed (on the surface ground) associated with the topographical lifting effect (black
 471 line in a - d, unit: m/s) and the boundary layer convergence effect (red line in a-d, unit: m/s) regulated by the topography (e - h, unit: m)
 472 (The red dashed line marks the range of the topography region)

473 6. Conclusion and Discussion

474 The long-term observation of geostationary satellite confirms that the mesoscale
 475 convection activities are highly active in the latitude zone of 30° N, where most of
 476 YRB is located. Different terrains distributed within the YRB play a significant role in
 477 the generation and the reinforcement of both eastward-moving MCSs and EMSV. The
 478 eastward-moving MCSs and the EMSV are mutually coupled and evolved into
 479 multi-scale EMSV systems during the eastward moving of the synoptic system.
 480 Among these complex terrain regions, the SSTR located in the eastern part of the
 481 Sichuan Basin is responsible for the significant strengthening of multi-scale EMSV
 482 systems when this type of synoptic system passes over. In this paper, we have focused
 483 on studying the mechanism of how the topographical effect of SSTR govern the
 484 evolution of the multi-scale EMSV system and its associated precipitation from the
 485 perspective of PV theory.

486 Three multi-scale EMSV system cases with similar origin locations, similar

487 cyclonic circulation scale, and same moving direction are selected from those high
488 impact weather events occurred in 2015 and 2016. The WRF simulation targeted for
489 the synthesis of these selected multi-scale EMSV system cases is capable in reflecting
490 the common evolution characteristics of the multi-scale EMSV system and the
491 common topographical effect of SSTR on the synoptic system. Based on the PPVI
492 theory, the compound circulation simulated by WRF is decomposed into the balanced
493 circulation and the perturbed circulation. The analysis of the two different types of
494 circulations mentioned above provides a distinctive insight into the topographical
495 effect of SSTR. The results indicate that the balanced circulation well capture the
496 meso- α scale cyclonic circulation, which provides the essential moisture condition for
497 the occurrence of the local heavy precipitation, while the perturbed circulation mainly
498 demonstrated local scale cyclonic feature, which provides the direct dynamic
499 condition for the occurrence of the local heavy precipitation. Moreover, the perturbed
500 circulation has quicker response to the topographical force than the balanced
501 circulation. The good agreement between the cyclonic feature of the perturbed
502 circulation and the distribution of the local heavy precipitation confirms that the
503 cyclonic perturbed circulation is conducive to the occurrence of the local heavy
504 precipitation. Further analysis shows that the persistence of the cyclonic perturbed
505 circulation is closely associated with the positive PV anomalies. Therefore, the
506 mechanism of how the positive PV anomalies are generated under the topographical
507 effect of SSTR becomes the key issue to be addressed here.

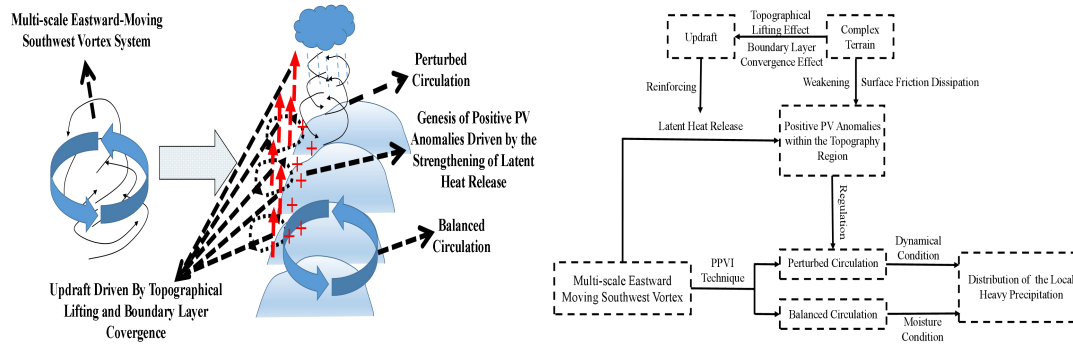
508 By performing a series of sensitivity experiments, the factors including the latent

509 heat release, the vertical wind and the relative vorticity are confirmed to have critical
510 roles in the genesis of positive PV anomalies. Besides, the sensitivity experiment on
511 the topographical elevation illustrates that the topographical effect has an indirect
512 impact on the genesis of positive PV anomalies mainly by reinforcing the factors
513 mentioned above. Also, it is found in the sensitivity experiment that the surface
514 frictional dissipation effect on the genesis of the positive PV anomalies is strictly
515 limited below 850 hPa isobaric surface. Then the quantitative diagnosis is performed
516 to validate the findings revealed by the sensitivity experiments. It is reported in
517 previous study that the source of the PV anomalies primarily includes two aspects:
518 One is origin from the latent heat release driven by the vertical wind (denoted by the
519 vertical velocity term), another one is origin from the latent heat release driven by the
520 horizontal eddy flow (denoted by the absolute vorticity term). The diagnosis results
521 show that the topographical force can reinforce both of these two aspects. However,
522 the latent heat release driven by the vertical wind contributes more to the temporal
523 variability of PV in the topography region than that driven by the horizontal eddy flow.
524 Further diagnosis is performed to explore the linkage between the vertical wind and
525 the topographical effect. The results show that both the topographical lifting effect
526 and the boundary layer convergence effect do have impacts on the variation of the
527 vertical wind, but the former one is the dominant mechanism whereas the latter one is
528 the secondary mechanism for the strengthening of the updraft by the quantitative
529 contrast of the two effects. Finally, to provide an intuitive understanding of the
530 revealed mechanisms, all the above findings are briefly visualized with the schematic

531 diagram and the associated illustration shown in Fig. 14.

532 Several new findings regarding the topographical effect of SSTR on the
533 multi-scale EMSV system are revealed in this paper, this research not only broadens
534 the understanding of the interaction mechanism between the complex terrain and the
535 PV anomalies, but also provides an innovative approach to reveal the topographical
536 effect on the multi-scale EMSV system from the perspective of PV theory. The
537 findings regarding the topographical effect in this paper highlight the topographical
538 lifting mechanism of the windward slope. Compared to the previous research on the
539 topographical lifting mechanism, the innovation of this paper lies in that it has
540 revealed the indirect connection between the topographical lifting mechanism and the
541 occurrence of the local heavy precipitation, from the perspective of PV theory, we
542 have respectively revealed the mechanism of how the topographical effect causes the
543 PV anomalies and how the PV anomalies govern the evolution of the multi-scale
544 EMSV system, ultimately the indirect connection between the topographical lifting
545 mechanism and the occurrence of the local heavy precipitation is effectively built
546 based on the above analysis. Despite some innovative findings revealed in this paper,
547 there are still some limitations existing in the present analysis. Firstly, the analysis
548 based on the synthesized simulation of these selected cases only revealed some
549 common features of the topographical effect on the multi-scale EMSV cases with long
550 lifespan, yet the characteristics of those ones with short lifespan are remained to be
551 studied. Thus future study on the topographical effect on the short lifespan EMSV is
552 required. Secondly, the study in this paper is focused on revealing the topographical

553 effect on the genesis of the PV anomalies. Still, the results may vary in terms of
554 different categories of topographical force. To be specific, the study only reveals the
555 topographical effect of the windward slope on the multi-scale EMSV system, but the
556 topographical effect associated with other topographies in SSTR, such as leeward
557 slope, mountain valley, may be vastly different from the windward slope, so further
558 study is demanded to thoroughly understand the topographical effect of SSTR. Finally,
559 the study in this paper only investigates the mechanism of how the topographical
560 effect affects the evolution of the balanced circulation and the perturbed circulation
561 respectively. However, the mutual coupling of the balanced circulation and the
562 perturbed circulation determines the crucial role of the interaction between these two
563 different types of circulation in the evolution of multi-scale EMSV system, but the
564 study on the mechanism of how the topography affects the interaction mechanism is
565 not involved in this paper. Therefore, it is also required further investigation on how
566 the topographical effect affects the interaction mechanism between these two different
567 types of circulation. In brief, more in-depth research on the interaction mechanism
568 between different types of the decomposed circulation, and more overall investigation
569 of the topographical effect associated different multi-scale EMSV systems and
570 different topographies within SSTR are in demand in order to better understand the
571 topographical effect of SSTR in the future.



572 Figure 14 The schematic diagram (left) and the associated illustration (right) of how the topographical effect govern the evolution of the
 573 multi-scale EMSV system and its associated precipitation from the PV theory

574 **Acknowledgments.** This work was supported jointly by the Integration Project of
 575 Major Research Program of National Natural Science Foundation of China (Grant nos.
 576 91937301), the National Natural Science Foundation of China (Grant nos. 41975058,
 577 4210050695) and the National Key R&D Program of China (Grant no.
 578 2018YFC1507200). The original FNL data are available from the RDA
 579 (<https://rda.ucar.edu>) in dataset number ds083.2. The CMORPH hourly fusion
 580 precipitation data were downloaded from the National Meteorological Information
 581 Center (<http://data.cma.cn>).

582 **References**

- 583 A. Eliassen, E. Krishnamurti (1957). Dynamic meteorology. Berlin: Handbuch der Physik,48,112-129.
- 584 C. A. Davis and T. J. Galarneau JR (2009). The vertical structure of Mesoscale Convective Vortices. *J. Atmos.*
585 *Sci.*,66:686-704.
- 586 C. G. Rossby (1940). Planetary flow patterns in the atmosphere. *Q. J. R. Meteorol. Soc.*,66,68-87.
- 587 C. Li, Y. Li, X. Jiang (2015). Statistical characteristics of the inter-monthly variation of the Sichuan Basin Vortex
588 and the distribution of daily precipitation. *Chinese Atmos. Sci.*, 39 (6): 1191–1203.
- 589 C. Schar and D. R. Durran (1997). Vortex formation and vortex shedding in continuously stratified flows past
590 isolated topography. *J. Atmos. Sci.*,54:534-554.
- 591 C. Schar, M. Sprenger, D. Luthi, et al (2003).Structure and dynamics of an Alpine potential-vorticity banner. *Q. J.*
592 *R. Meteorol. Soc.*,129:825-855.
- 593 C. Yue, J. Li, P. Chen, et al (2013). Study on improvement of moist Q vector interpretation technique. *Chinese*
594 *Plat. Meteor.*, 32(6):1617-1625.
- 595 D. J. Raymond and H. Jiang (1990). A theory for long-lived mesoscale convective systems. *J. Atmos.*
596 *Sci.*,47(24):3067-3077.
- 597 D. J. Raymond (1992). Nonlinear balance and potential vorticity thinking at large Rossby number, *Q. J. R. Meteor.*
598 *Soc.*,118:987-1015.
- 599 D. Zhang and C. Q. Kieu (2006). Potential vorticity diagnosis of a simulated hurricane. Part II:quasi-balanced
600 contributions to forced secondary circulations. *J. Atmos. Sci.*,63:2898- 2914.
- 601 E. J. Mlawer, S J Taubman, P D Brown, et al (1997). Radiative transfer for inhomogeneous atmospheres: RRTM, a
602 validated correlated-k model for the longwave. *J. Geophys. Res. Atmos.*,102(D14): 16663-16682.
- 603 G. T. Chen, C. C. Wang, S. C. Liu (2003). Potential vorticity diagnosis of a Mei-Yu front case. *Mon. Wea.*
604 *Rev.*,131:2680-2696.
- 605 H. Ertel (1942). Ein neuer hydrodynamischer Erhaltungssatz. *Die Naturwissenschaften*,36,543-544.
- 606 J Dudhia (1989). Numerical study of convection observed during the Winter Monsoon Experiment using a
607 mesoscale two-dimensional model. *J. Atmos. Sci.*,46(20): 3077-3107.
- 608 J. A. Milbrandt, & M. K. Yau (2005). A multimoment bulk microphysics parameterization. Part II : A proposed
609 three moment closure and scheme description. *J. Atmos. Sci.*, 62, 3065-3081.
- 610 J. G. Charney (1955). The gulf stream as an inertial boundary layer. *PNAS*, 41(10):731-740.
- 611 J. Ge,W. Zhong ,Hancheng Lu (2011). Diagnostic analysis of the quasi-balanced flow of a mesoscale vortex during
612 the 12 June 2008 Guangxi Rainstorm.*Acta Meteorological Sinica*,25:188-202.
- 613 J. Sun, F. Zhang (2012). Impacts of mountain-plains solenoid on diurnal variations of rainfalls along the Mei-Yu
614 front over the East China Plains. *Mon. Wea. Rev.*,140:379-397.
- 615 L. Zhang, J. Min, X. Zhuang, et al (2019). General Features of Extreme Rainfall Events Produced by MCSs over

616 East China during 2016-2017. *Mon. Wea. Rev.*, 147: 2693-2714.

617 P. A. Jimenez, J Dudhia, J F Gonzalez, et al (2012). A revised scheme for the WRF surface layer formulation. *Mon.*
618 *Wea. Rev.*,140:898-918.

619 P. H. Haynes and M. E. McIntyre (1987). On the evolution of vorticity and potential vorticity in the presence of
620 diabatic heating and frictional or other forces. *J. Atmos. Sci.*,44:828-841.

621 Q. Wang and Z. Tan (2009). Idealized numerical simulation study of the potential vorticity banners over a
622 mesoscale mountain: dry adiabatic process. *Adv. Atmos. Sci.*,26:906-922.

623 R. A. Houze Jr (2004). Mesoscale convective systems. *Rev. Geophys.*, 42, doi:10.1029/2004RG000150.

624 R. Yang, Y. Zhang, J. Sun, et al (2019). The characteristics and classification of eastward-propagating mesoscale
625 convective systems generated over the second-step terrain in the Yangtze River Valley. *Atmos. Sci.*
626 *Lett.*, 20:e874.

627 S. Fu, Z. Mai, J. Sun, et al (2019). Impacts of convective activity over the Tibetan Plateau on Plateau Vortex,
628 Southwest Vortex, and downstream precipitation. *J. Atmos. Sci.*, <https://doi.org/10.1175/JAS-D-18-0331.1>.

629 S. Y. Hong, Y Noh, J Dudhia (2006). A new vertical diffusion package with an explicit treatment of entrainment
630 processes. *Mon. Wea. Rev.*,134(9):2318-2341.

631 T. M. Peter, J H Greg (1999). The role of potential vorticity generation in tropical cyclone rain bands. *J. Atmos.*
632 *Sci.*, 56:1224-1228.

633 W. Cui, X. Dong, B. Xi and M. Liu (2020). Cloud and precipitation properties of MCSs along the Meiyu frontal
634 zone in central and southern China and their associated large-scale environments. *J. Geophys. Res. Atmos.*
635 *Atmos.* 125(6), <https://doi.org/10.1029/2019JD031601>.

636 X. Wang and D. Zhang (2003). Potential vorticity diagnosis of a simulated hurricane. Part I: formation and
637 quasi-balanced flow. *J. Atmos. Sci.*,60:1593-1607.

638 X. Yang, J. Fei, X. Huang, et al (2015). Characteristics of Mesoscale Convective Systems over China and its
639 vicinity using geostationary satellite FY2. *J. Climate*, 28: 4890-4907.

640 Y. Shen, A. Xiong, Y. Wang, et al (2010). Performance of high-resolution satellite precipitation products over
641 China. *J. Geophys. Res.*,vol.115, D02114, doi:10.1029/2009JD012097.

642 Y. Zhang, F. Zhang, C. A. Davis, et al (2018). Diurnal evolution and Structure of long-lived mesoscale convective
643 vortices along the Mei-Yu front over East China Plains. *J. Atmos. Sci.*,75:1005-1025.

644 Y. Zhao, Z. Li, Z. Xiao, et al (2008). A PV inversion diagnostic study on a quasi-stationary Meiyu front with
645 successive rainstorms. *Acta Meteorologica Sinica.*,65(3):353-371.

646 Y. Zheng, J. Chen, P. Zhu (2008). The distribution and diurnal variation of mesoscale convective systems occurred
647 in China and its surrounding area in summer. *Chinese Sci. Bull.*, 53(4):471-481.